Demonstrator Experiments on Significant Effects During Pile Installation

J. Vogelsang, G. Huber and Th. Triantafyllidis

Abstract Benchmark tests for the numerical simulation of pile installation require clearly defined boundary value problems with corresponding experimental data. These experiments have to provide quantitative information on the soil deformations and stresses. Large scale model tests in dry, granular soil were carried out for this purpose. The interface testing device, that is used for the tests, allows the investigation of selected aspects of pile penetration. The normal and shear forces on the pile structure are measured. The displacements in the surrounding soil zone can be evaluated via Digital Image Correlation (DIC). The test results concentrate on the interface behavior between the soil and the pile and the evolution of stresses and deformations around the pile tip. For rough pile surfaces the occurrence of dilatancy effects in the pile-soil interface is shown. The localization of deformations in the post-peak phase is analyzed for monotonic and cyclic test paths. The influence of the pile driving mode on the evolution of stresses around the pile tip is demonstrated.

Keywords Pile installation · Large scale model test · Benchmark test · Soil-structure interaction

1 Introduction

The research unit FOR 1136 has the objective to provide numerical tools for the simulation of pile driving processes. The main focus is on the installation of vibro-injection piles, in German RI-piles (Rüttelinjektionspfähle). Such piles are schematically illustrated in Fig. 1. RI-piles are H-section steel profiles that are vibrated into the ground. The collar, a welded flat-bar placed above the pile tip, displaces the soil and creates a cavity above. Simultaneously to the pile installation, cement grout is

J. Vogelsang (✉) · G. Huber · Th. Triantafyllidis
Institute of Soil Mechanics and Rock Mechanics, Karlsruhe Institute of Technology,
Karlsruhe, Germany
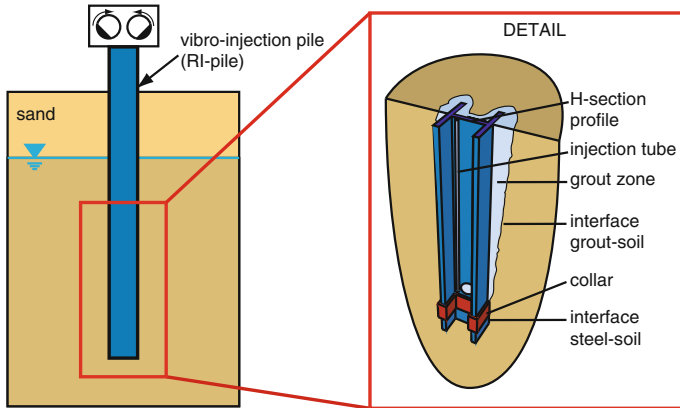e-mail: triantafyllidis@kit.edu

Fig. 1 Schematic illustration of RI-pile installation

injected into this cavity and encloses the steel profile. When cured, the grout offers a corrosion protection in combination with a rough contact to the surrounding soil.

These processes are influenced by several effects that have to be taken into account in simulations. Pile driving is a high-cyclic, dynamic process that often takes place in water saturated soil. This causes important liquefaction effects around the pile. The penetration of the pile structure induces large soil deformations that have to be handled using adequate simulation techniques. The interface between the soil and the pile structure has to be considered as well as the interaction between soil and cement grout. The influences of these aspects are difficult to separate, for real pile installations as well as in experiments. Therefore, demonstrator experiments on selected aspects have to be performed. The experimental investigations discussed here concentrate on the pile penetration in dry soil without grout injection. In this contribution, the requirements for these tests are defined, the test devices are illustrated and representative results are shown.

Many geotechnical model tests dealing with penetration of pile-like structures have been performed, mostly in dry granular soil in order to exclude pore water effects. E.g. [2] or [6] present experiments with small scale piles penetrated into dry sand. Usually the overall axial/vertical pile force is measured in relation to the penetration depth. In [2] the tip resistance and skin friction forces were extracted from the pile head force. Soil displacements are rarely evaluated in these kind of tests. Other experiments using glass windows installed in symmetry planes allow the observation of soil displacements, e.g. the model test performed in [1]. Another problem is the measuring of the stress distribution. In [9] a possible solution is presented, however, without evaluation of the soil displacements. The combination of extensive stress measurements and evaluation of the soil displacements in one experiment is a complex challenge. Such experiments were therefore only performed very rarely.

Often, the purpose of geotechnical model tests is a qualitative prediction on the behavior of real pile structures. As shown e.g. in [14], the quantitative application on real structures of results obtained from small scale tests is doubtful. Scaling effects can significantly limit the transferability of the test results. Some field tests that enable the application of test results on real pile structures have been performed. Examples are presented in [8] or [4]. Those tests eliminate scaling effects and are performed in the in-situ soil layers. The instrumentation is usually limited on the axial pile head force. In [8], in addition, a sophistically instrumental model pile allowed the evaluation of tip resistance and skin friction.

To provide experimental data for boundary value problems that can be back-calculated with numerical methods is another purpose of geotechnical model tests. Such experiments have to reproduce similar effects as the real process that is to be investigated. The test conditions have to be kept as simple as possible and an extensive instrumentation has to provide quantitatively reliable results on the evolution of stresses and deformations. It is useful to focus the experimental set-up on selected aspects (e.g. contact zone between the soil and the structure or liquefaction effects) and to exclude effects of secondary interest. These effects can rarely be separated in small scale tests. Large scale tests that simulate only parts of a real structure in a realistic scale are one possibility to solve this problem. Such model tests are presented in this paper.

A large scale interface testing device is used to investigate the soil-structure interaction for monotonic and cyclic test paths. A sophisticated instrumentation enables the measuring of shear and normal stresses in the interface for smooth and rough structural surfaces. The soil displacements are observable and can be evaluated by DIC.

The interface testing device is also used for tests on the penetration of pile-like structures under plane strain conditions. The test configuration and the instrumentation allow the observation of skin friction and tip resistance. Idealized tests simulating a 2D pile penetration are performed for the validation of FE-techniques. In the tests, the difference between the so-called cavitational and non-cavitational pile driving [2] and its influence on the soil deformation is shown.

2 Interface Test Device

The interface test device used for the tests has already been presented in detail in [10, 13]. Nevertheless, for a better comprehension of the following recent results, we will recapitulate the essential aspects.

2.1 Basic Idea

The basic idea of the interface test device is the transition of an idealized pile structure into plane structures that are investigated separately. In Fig. 2a an idealized pile
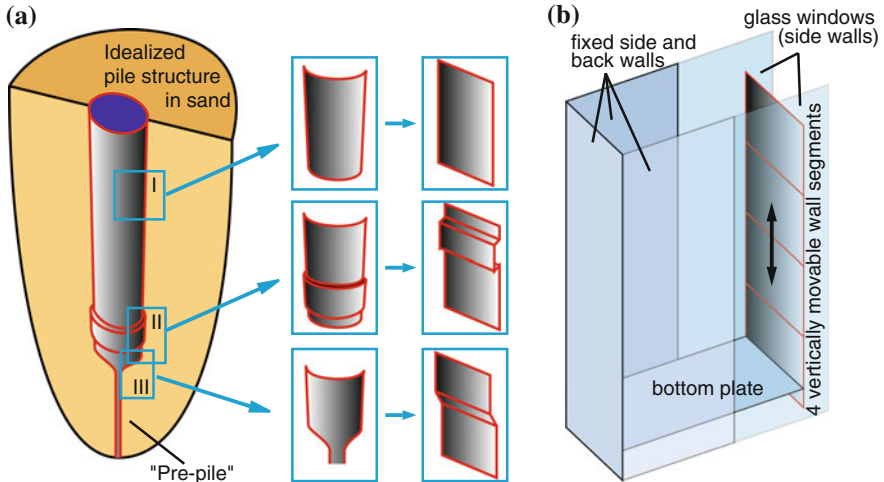
Fig. 2 Interface testing device—basic idea. **a** Transition of sections of an idealized pile structure to 2D wall elements. **b** Schematic design of the interface test device

structure is shown. The idealized pile is simplified to a radial symmetric structure that is penetrated into sand. This simplified pile has skin sections (detail I), structural elements imitating the collar of an RI-pile (detail II) and a pile tip (detail III).

As in many numerical simulations the pile has a "pre-pile" with a small diameter compared to the pile. The pile itself represents only an expansion of this pre-pile. In the interface test device parts of this idealized radial symmetric structure are cut out and "unfolded" to plane elements. This transition is illustrated in Fig. 2a. The plane pile elements are integrated in the interface test device as wall segments, Fig. 2b. The wall segments are guided and can be moved vertically between two glass windows placed on the side. The back part of the test device is designed with stiff construction plates. A bottom plate forms the lower boundary of the box and the sand filling. In the tests, the wall segments interact with the sand and are displaced vertically performing various test paths. The sand displacements can be observed through the glass windows on the sides. The forces acting between the sand and the wall segments are measured by load cells integrated in the supports of the wall segments. In that way, both, displacements and stresses in the zones of interest, are evaluated.

2.2 Design

Figure 3a shows a side view on the interface test device. Some design details are shown schematically in Fig. 3b. More technical details are discussed in [13].

A stiff outer steel construction minimizes the deformations of the test device and their influence on the experiments. From the outside, the back part of the sand body
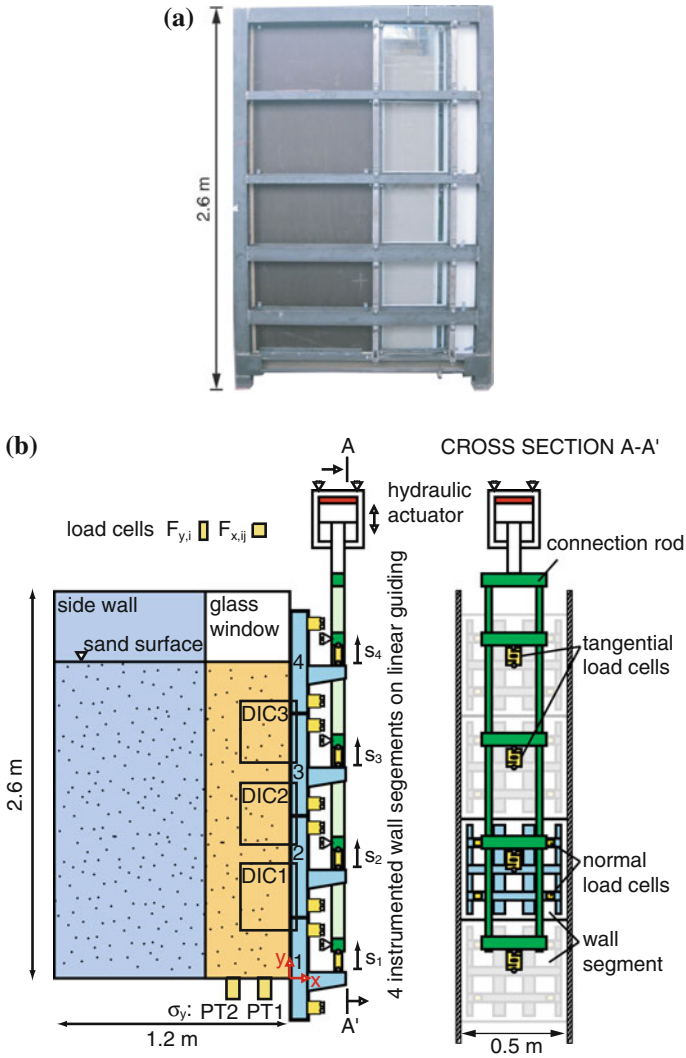
Fig. 3 Overview—interface test device. **a** Side view and **b** schematic side view and view on the back side of the wall segments

is hidden by side walls, only the first part in vicinity to the wall segments is visible through glass windows (on the front and on the back side). Between the horizontal steel beams five fields with free view on the sand body can be used to take image sequences during the tests. Usually, the three middle windows are used (named DIC1, DIC2 and DIC3 in Fig. 3b).

The base area of the sand filling is $1.2\,m \times 0.5\,m$. Sand heights up to $2.0\,m$ are possible. Usual sand heights range between 1.5 and $1.7\,m$. The movable wall is

divided into four instrumented segments (numbered 1–4 from bottom to top). The wall segments are based on a stiff steel frame in order to minimize their deformations. The front plates of the wall segments are modifiable and can be adapted depending on the test configuration. Each wall segment has load cells for the measuring of the normal and the tangential (vertical) force acting on the front plate, see below. The wall segments are coupled separately to a ladder-like connection rod. The view on the back side of the wall segments in Fig. 3b illustrates their position relative the connection rod. The second segment is highlighted. A hydraulic actuator is placed on top of the test device and moves the connection rod in vertical direction. The maximum possible wall displacements are about 200 mm.

2.3 Test Configurations

Various test configurations are possible in the interface test device. Three basic configurations for the simulation of pile driving can be distinguished and were investigated, Fig. 4.

Configuration I focuses on the cyclic and monotonic interface behavior between the soil and the pile. In this configuration four plane wall segments with modifiable surface roughness are installed. In the tests presented here, the segments 1, 3 and 4 have smooth surfaces of stainless steel, while segment 2 has a rough surface (sanded steel). The wall segments represent a part of the skin section of a pile.
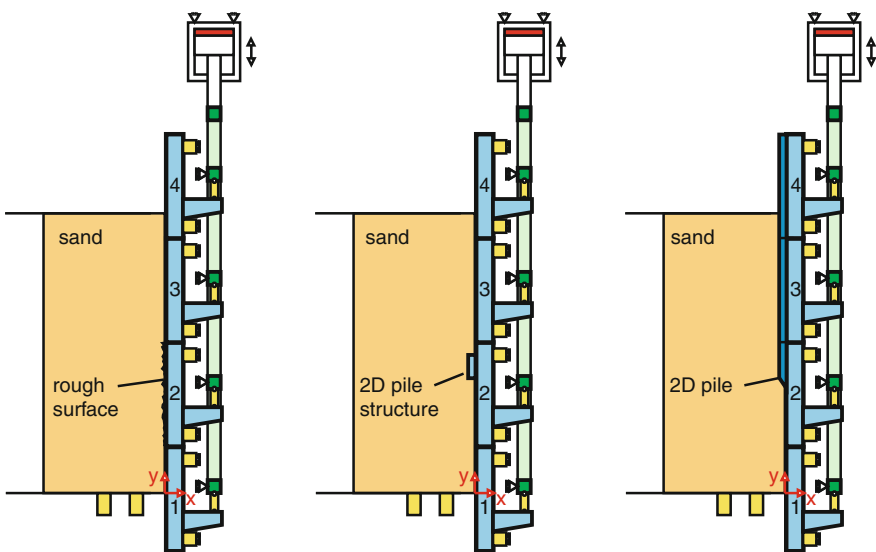

Fig. 4 Basic test configurations in the interface test device

Configuration II investigates the influence of structural geometries more similar to real pile structures. The segments are installed with smooth steel surfaces. A pile structure imitating the collar of RI-piles is mounted on segment 2. The tip resistance on this structure can be evaluated. In addition to this, its influence on the skin friction on the upper segments can be observed as well.

Configuration III represents a 2D pile and is particularly suited for the validation of numerical simulations of the pile penetration problems. Segment 2 contains an inclined pile tip. Segment 3 and 4 are shifted into the test device and form a complete pile in 2D in combination with segment 2.

2.4 Instrumentation

The test device provides a sophisticated instrumentation. The basic instrumentation installed in the test device is presented in [10]. The more advanced instrumentation of the test device which has been added in a later stage of development is discussed in [13]. Here, an overview of the instrumentation components is provided, Fig. 3.

Tangential Forces $F_{y,i}$. Each wall segment is attached individually to the connection rod by one tangential load cell (HBM RSCA). In the case of plane wall segments, the tangential load cell generally measures the resulting shear force on the front plate and furthermore a weak systemic friction force of the Teflon sealings on the glass windows. In the case of segment 2 in the test configurations II and III, a tip force under the pile tip is also included in the tangential force.

Normal Forces $F_{x,ij}$. In the basic version of the test device [10], the measuring of the normal forces on the wall segments was not possible. However, for the usage as demonstrator experiments for the validation of contact formulations, the knowledge of normal stresses in the contact zone is crucial, but its measurement in granular soil is complex. The measuring elements have to be very stiff in order to avoid a significant influence on the earth pressure. Due to high quality and stiffness requirements in combination with geometric constraints, the usage of commercial products was excluded. Thus, self-designed and fabricated load cells are used. Their construction is discussed in detail in [13]. Four load cells per segment are integrated between the steel frame and the guidings. Usually, the sum of all four load cells $F_{x,ij}$ per segment is shown in the results ($F_{x,i}$: resulting normal force on segment i).

Displacements s_i. The non-uniform force distribution on the wall segments leads to different deformations of the tangential load cells, ergo varying displacements of the wall segments. Therefore, the displacements are measured separately with one absolute magnetostrictive position transducer (Novotechnik TLM 300) per segment.

Vertical Stress σ_y. Two pressure transducers measure the evolution of the vertical stresses on the bottom plate. They are integrated centrically into the bottom plate with a horizontal distance to the wall segments of 0.15 m (PT1) and 0.30 m (PT2). Pressure transducers with very stiff front membrane are used (VEGABAR 52).

2.5 Evaluation of Soil Displacements

Image Sequences. The first part of the side walls is constructed with glass windows. Thus, between the horizontal steel beams the contact zone between the wall and the soil is kept visible throughout the tests. During the tests three digital cameras take image sequences in the fields DIC1, DIC2 and DIC3, Fig. 3. The arrangement of the cameras on the side of the device is illustrated in detail in [13].

The obtained image sequences are preprocessed digitally before the DIC evaluation. The images are rotated in order to precisely place the wall in a vertical orientation. Only the zone of interest (sand without steel beams) is evaluated subsequently. The edges of the wall segments (where the displacements s_i are measured) are kept in this zone in order to allow a control of the calculated displacements.

Digital Image Correlation (DIC). The freeware code JPIV [12] is used to evaluate the incremental displacement fields by comparing every pair of consecutive images in the recorded image sequences. Many recommendations can be found in the literature for the settings in DIC evaluations [15, 16]. The settings chosen here are in accordance with these. The vector spacing (width and height of the search patch) is set to 12–16 pixel ($4-5 \times d_{50}$). Thus, the search patch contains enough pixel and sand grains for a good precision and it enables the visualization of localized deformations (shear band width about $10 \times d_{50}$, see below).

After the JPIV evaluation invalid vectors are marked by a "normalized median test" and replaced by the median of the neighboring vectors. Invalid vectors are marked if their displacement differs too much compared to the neighboring vectors (details in [12]). Invalid vectors can occur in areas of the image that provide only low texture. In this particular application the problematic zones are on the edges of the wall segments and especially the teflon sealings. In the evaluations presented, the number of invalid vectors was very low (maximum 3 per image evaluation). If appropriate settings are used invalid vectors in the sand zone do not occur.

From the JPIV analysis ASCI-files containing the incremental displacements (image n and n+1) are obtained. Subsequently, these displacements are summated to the cumulated displacements and the deformations are calculated.

3 Test Results

3.1 Configuration I: Soil-Pile Interface Behavior

The soil-pile interface behavior was investigated with a series of tests using the first configuration (plane wall segments). In this test configuration, the segments 1, 3 and 4 were installed with smooth steel surfaces. Segment 2 has a rough (sanded) surface. Monotonic tests were performed as well as cyclic tests with different test paths. Here, a cyclic test is compared to a test performing a monotonic wall displacement. The

initial conditions were similar in both tests with about 1.5 m sand height and an initial relative density of $I_D \approx 65\%$. The initial conditions and test paths are schematically illustrated in Fig. 5a, b.

A wall displacement of 57 mm downwards is imposed in the monotonic test. In total, the cyclic test performing an alternating wall displacement reaches also 57 mm wall displacement. The alternating displacement was carried out using the following progression sequence: first 11 cycles of 3 mm down and 1 mm up and afterwards 7 cycles of 5 mm down and 1 mm up.

The Fig. 5c–e compare the results of both tests. The evolution of the tangential force on the second wall segment is shown in Fig. 5c. In the cyclic test (blue curve) the tangential force increases over 3 cycles and reaches its maximum at 9 mm displacement. In the pull-out phases the tangential force vanishes in all cycles, except the first. In all other cycles the wall displacement of 1 mm is not enough for a reversion of the shear stresses. In the monotonic test (red curve) the tangential force increases slightly stronger on the first 6 mm. After 6 mm displacement the curve kinks, cuts the peak of the cyclic curve and behaves like an envelope in the residual test path.

Both tests show a peak in the curve of the normal force, Fig. 5d. The peak occurs after 9 mm in the monotonic and after 11 mm in the cyclic case. The normal force in the monotonic test envelopes the curve of the cyclic test. The normal force does not vanish in the pull-out phases because in granular soil a minimum earth pressure has to be maintained.

Since normal force $F_{x,2}$ and tangential force $F_{y,2}$ act on the same area, the mobilized friction angle on the segments surface δ_{mob} can be calculated as follows:

$$\delta_{mob} = \arctan(F_{y,2}/F_{x,2}). \tag{1}$$

The cyclic test shows a global maximum of $\delta_{mob} = 39°$ after 7 mm displacement. Furthermore, in all subsequent cycles a small peak is mobilized. The residual value of δ_{mob} is about 35°. The monotonic test shows an earlier peak after 4 mm displacement. Its maximum is about 38°. The residual value ranges between 33 and 36° and corresponds approximately to the residual values of the cyclic test. In neither case a critical state is reached ($\varphi_{c,sand} = 33°$ from drained triaxial tests).

The results shown in Fig. 5 become more clear when the soil displacements obtained from DIC are considered. The displacement vectors of the monotonic test are plotted in Fig. 6a for a small horizontal cross section in the interface zone between the rough wall segment 2 and the sand. The accumulated displacements are shown for the monotonic test at the peak of the mobilized friction angle (s = −3.5 mm), after the peak (s = −6.0 mm about at the kink of $F_{y,2}$), at the global minimum (s = −8.5 mm about at the peak in $F_{x,2}$) and after a large displacement of s = −20 mm. For the cyclic test the accumulated displacements are shown at similar wall positions in Fig. 6b. The position s = −3.5 mm is now before the peak, s = −5.8 mm about at the peak and s = −8.5 mm just after it. A displacement of s = −20.4 mm still corresponds to a position on the residual path.

Figure 6a reveals that the displacement field is smooth until the peak of δ_{mob} is reached. The displacements constantly decrease at larger distances from the wall
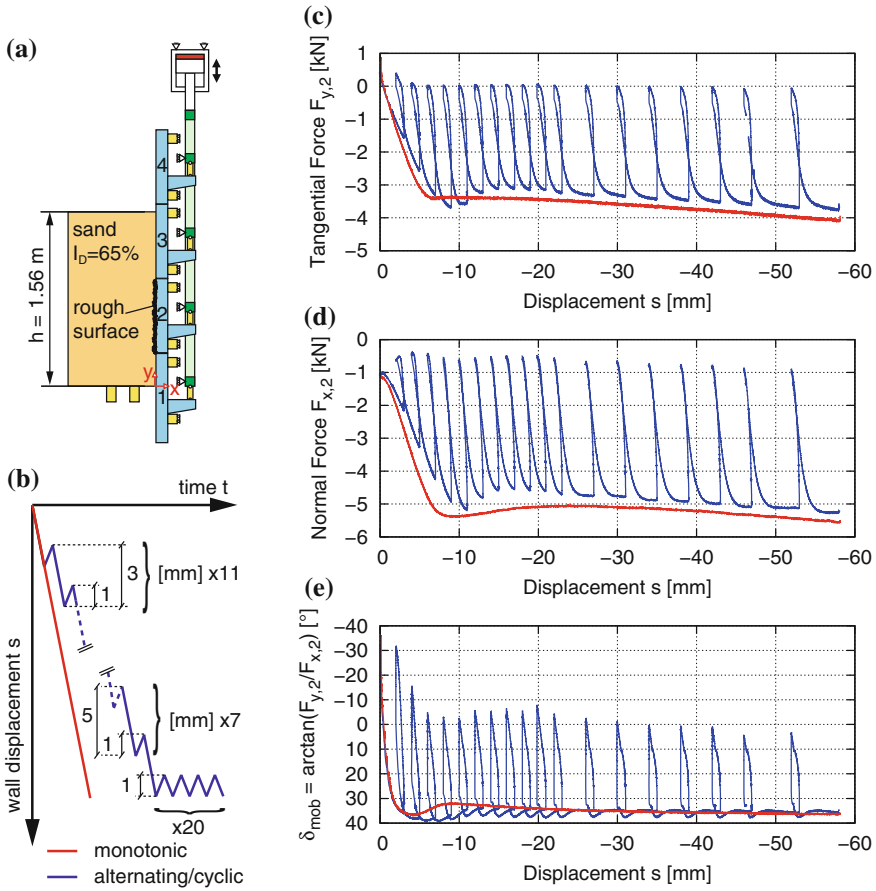
Fig. 5 **a** Initial conditions, **b** test paths and **c–e** tangential force $F_{y,2}$, normal force $F_{x,2}$ and mobilized friction angle $\delta_{mob} = \arctan(F_{y,2}/F_{x,2})$ on 2nd segment over wall displacement

segment. The deformations are more or less homogeneous. After the peak, an increase of the displacements near the segment surface can be observed. The deformations start to localize in a shear band in front of the wall segment. After 8.5 mm wall displacement, the zone with large gradients is already more pronounced. It becomes evident after a large displacement of 20 mm. The zone of large localized deformations consists in a band of about 5–6 mm in width. This corresponds to approximately 9–11 times the mean grain diameter d_{50} ($d_{50} = 0.55$ mm). The slight drift of the displacement vectors to the left, beginning from the fourth vector (from the right), indicates a dilative soil behavior in the shear band. The post peak behavior with the beginning of strain localization was already reported, e.g. for triaxial tests in [5, 11] or for various model tests in [7].

Fig. 6 Displacement vectors for **a** the monotonic and **b** the cyclic test in a horizontal cross section at y = 955 mm
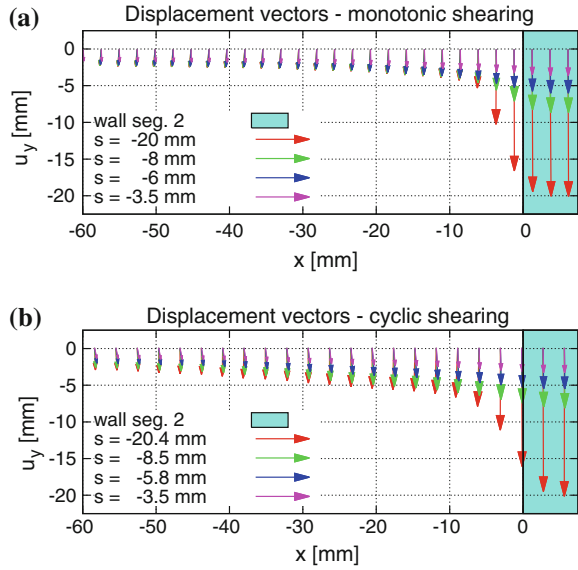
The cyclic test shows similar displacement vectors but the localization occurs later, Fig. 6b. After 8.5 mm wall displacement, the deformations are still homogeneous. Also for the cyclic test, the strain localization corresponds to the peak of δ_{mob}. For 20 mm displacement the shear band in front of the wall segment can clearly be distinguished. The width of the shear band is similar to the monotonic case. With about 7 mm in width, it is a bit larger than in the monotonic case. This width corresponds to approximately 12–13 times the mean grain diameter d_{50}.

In the case of the cyclic test, after the wall displacement sequence downwards a cyclic wall displacement with constant amplitude of 0.5 mm was performed. 20 cycles were performed. Figure 7 plots the averaged tangential (shear) stress over the normal stress for selected cycles. The averaged stresses are the tangential and normal forces $F_{y,2}$ resp. $F_{x,2}$ divided by the surface area of the interface zone (0.3 m^2). This presentation is equivalent to the averaged $\tau - \sigma$-plane in the interface between the soil and the wall. The two critical state lines (CSL) are plotted with $\varphi_c = 33°$. In the bottom left corner of each subfigure, the test path and the current position are indicated schematically. The current cycle is highlighted in red. The previous test path is illustrated in grey with continuous line and the subsequent test path with a grey dotted line. The force path is presented analogously. Small arrows illustrate the curve orientation.

Figure 7a shows the last phase large displacements downwards of the previous test path. Both, tangential and normal stress, increase significantly and exceed the CSL. In the first cycle, the tangential stress drops to zero, Fig. 7b. The end of the first cycle corresponds to the preceding phase of large displacement downwards. In Fig. 7c a strong relaxation of both stresses can be observed for the second cycle. The cycle ends on the CSL. After five cycles a relaxation can still be observed, however, at a
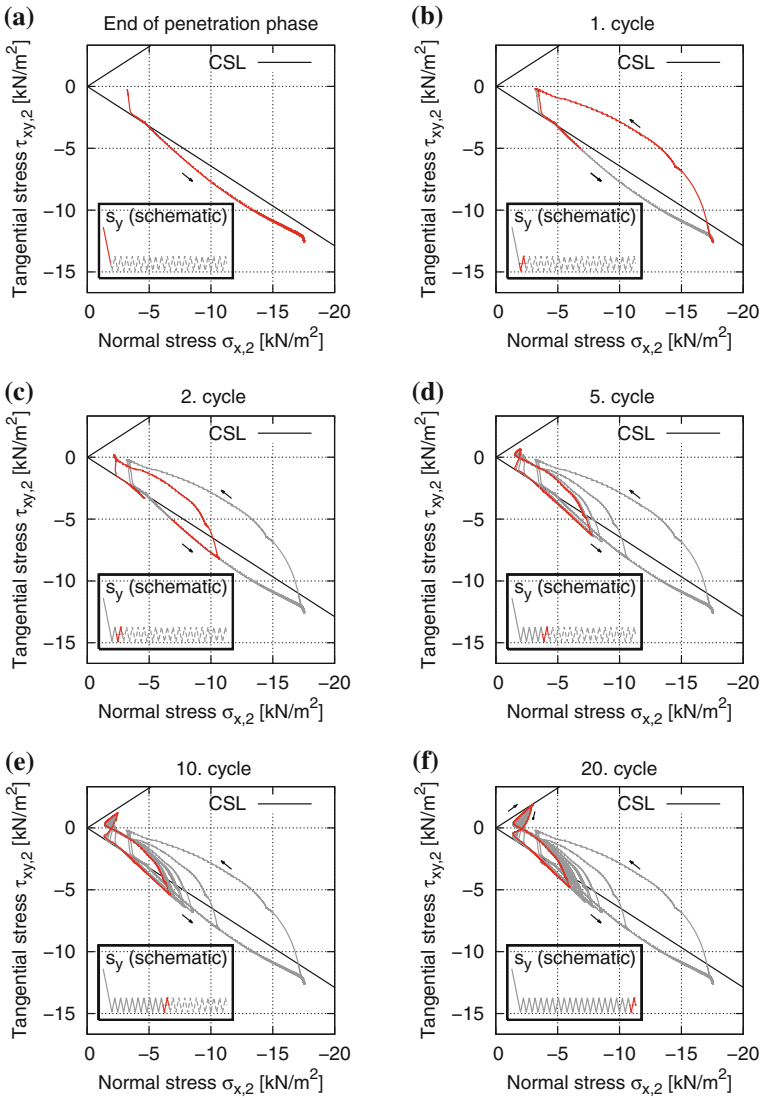
Fig. 7 Tangential stress $\tau_{xy,2}$ over normal stress $\sigma_{x,2}$ for cyclic wall displacement with $s_{\text{ampl}} = \pm 0.5\,\text{mm}$

lower rate. In the pull-out phase, the tangential stress starts to reverse and a butterfly curve shape forms. In the following cycles, the penetration phases are similar to the preceding cycles with only slight relaxation. However, in the pull-out phases, a stronger stress reversion takes place (Fig. 7e, f).

Figure 7 clearly reveals the soil-like behavior of rough interfaces. Contractancy and dilatancy effects have to be modeled by contact formulations if the interaction

is of primordial importance for the simulation. For pile penetration problems this is assumed to be the case in the region close to the pile tip and along the pile shaft (in the case of non-injection piles).

3.2 Configuration II: Estimation of the Tip Resistance

The results of a test using configuration II are shown in order to illustrate the influence of the pile driving mode for dense sand. The initial conditions and the test path are given in Fig. 8a. The test path corresponds to an alternating penetration of 57 mm in total. After 20 mm, two small cycles with 0.5 mm movement upwards are performed. In comparison to these small cycles, three larger cycles (5 mm upwards) are performed after 40 mm wall penetration. The presented results concentrate on the effects around the 2D pile tip installed on the second segment.

Figure 8b shows the tangential force $F_{y,2}$ on the second segment (with pile tip) over the wall displacement. The arrows indicate the curve progression. After about 10 mm wall displacement, the tangential force increases almost asymptotically. The two small cycles lead to a slight reversion of the tangential force up to about 0.25 kN. The response after the pull-out phases is stiff. The asymptotic envelope curve is already reached 4 mm after the last reversal point. The larger cycles are significantly different. In the pull-out phases a value of 0.25 kN is rapidly reached and remains constant throughout the whole phase. After the pull-out phase, the tangential force almost instantaneously changes direction to a negative value of -0.4 kN. Subsequently, the force remains approximately constant for 2 mm of penetration before it restarts to increase. The increase is much slower compared to the small cycles. The soil behavior is significantly softer. 4 mm additional displacement in these cycles are not enough to reach the asymptotic curve of the previous penetration.

Evidently, the evolution of the tangential force is a result of the soil behavior under the 2D pile tip (collar). The tip force cannot be measured directly in the current configuration but it can be evaluated from the measured forces.

The force distribution on wall segment 2 is illustrated in Fig. 9 for displacements downwards and upwards.

The tangential force $F_{y,2}$, measured by the tangential load cell, is usually directed downwards in the penetration phases and upwards in the pull-out phases. The normal force $F_{x,2}$ is always a compressive force and enables the mobilization of friction on the wall segments surface. $F_{x,2}$ is measured via four normal load cells $F_{x,2} = \Sigma F_{x,2,i}$ ($i = 1-4$). The resulting friction force is named F_τ and can be estimated as follows:

$$F_\tau = \int^{A_{\text{seg}}} \tau \, dA = F_{x,2} \cdot \tan(\delta_{\text{mob}}), \qquad (2)$$

wherein A_{seg} is the surface area of the segment and δ_{mob} is the mobilized friction angle steel-soil. For large unidirectional displacements (>1 mm), this friction angle can be assumed to be fully mobilized ($\delta_{\text{mob}} = \delta_{\text{max}}$). The segments surface partly
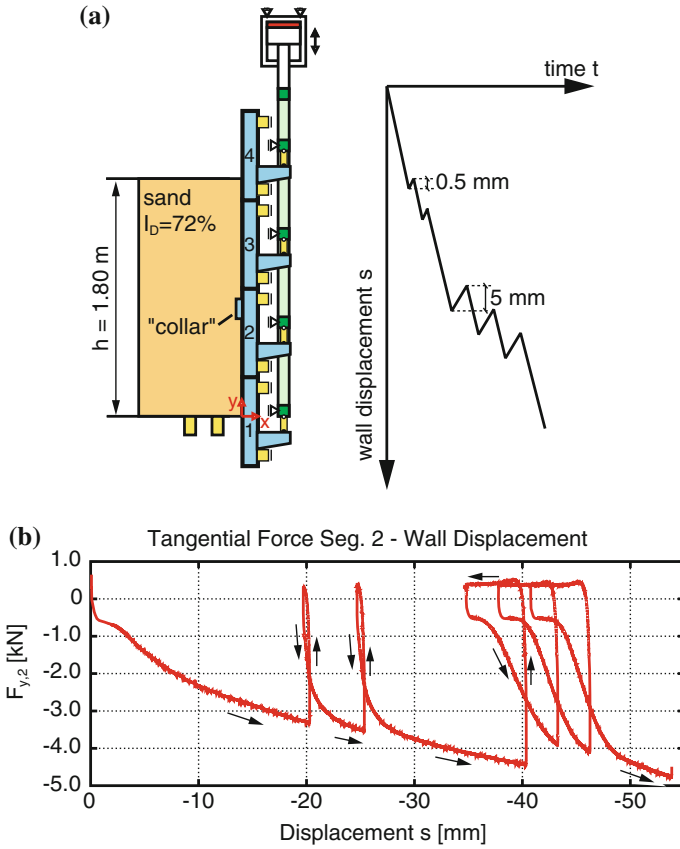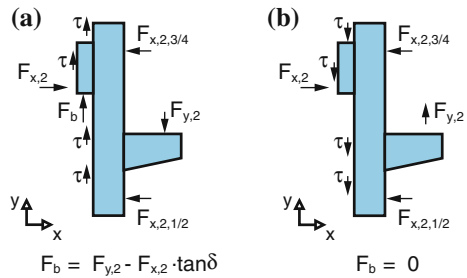
(a)

(b)

Fig. 8 V14-4—Alternating penetration in dense sand. **a** Initial conditions and test path and **b** tangential force $F_{y,2}$ on 2nd segment over displacement

Fig. 9 Force distribution on segment 2 for displacement **a** downwards and **b** upwards

consists of stainless (front plate) and partly of common steel (collar). For the stainless steel surfaces, δ_{max} can be measured on the smooth segments 1 or 3. Usually, values of about 13° are obtained. Taking the higher roughness of common steel into account, δ_{max} was estimated at 16° here. The friction force is directed against the

wall displacement, thus, against $F_{y,2}$. The last force to be considered is the tip force F_b. This force is always directed upwards and vanishes for large displacement in the pull-out phases.

Assuming that the friction angle is fully mobilized, the tip force can be estimated accurately. Taking the distinction of cases (displacements down- or upwards) into account, the absolute value of the tip force F_b can be calculated as follows:

$$|F_b| = |F_{y,2}| - |F_{x,2}| \cdot \tan(|\delta_{max}|) \quad (\Delta s \downarrow) \tag{3}$$

$$|F_b| = |F_{x,2}| \cdot \tan(|\delta_{max}|) - |F_{y,2}| \quad (\Delta s \uparrow). \tag{4}$$

Problems occur at reversal points in the test path. Just after changes of direction of the wall displacements, the mobilized friction angle is unknown. A characteristic line for its evolution after reversal points cannot be specified for all cases. Amongst others, it strongly depends on the stress state and the soil density. This problem is (yet) not solved at the moment. Thus, the tip force can only be roughly interpolated in the phases about 0.3–0.4 mm wall displacement after reversal points.

Figure 10 presents the calculated tip force obtained from Eqs. 3 and 4 for test V14-4. The sections calculated with Eq. 4 are plotted in red, those calculated with Eq. 4 in blue and the interpolated section in green.

The calculated tip force in Fig. 10 is comparable to the tangential force $F_{y,2}$ in Fig. 8b. However, there are important differences. In the small cycles, the tip force does not vanish. A minimum value of -0.4 kN remains in the top position of both cycles. 2D pile tip and sand are always in contact. In the new penetration phases, the tip force first increases rapidly. Exceeding the lowest previous position, the response gets softer and the curve approaches the asymptotic penetration envelope curve. In the larger cycles in contrast, the tip force evolutes in a different way. A complete stress relief under the 2D pile tip is reached after a displacement upwards of about 1.5 mm. A loss of contact between pile tip and sand was observed in these phases during the test. In the new penetration phases, there is still no tip force for about 2 mm displacement. This penetration is necessary to close the gap between pile tip and sand surface. Afterwards, the tip force slowly restarts to increase with a much softer response than in the small cycles.

From Fig. 10 can be concluded that the evaluation of the tip force following Eqs. 3 and 4 works correctly in the given case. A strong argument in favour of this conclusion is that in the phases without contact between tip and sand zero tip force is calculated with Eq. 3 as well as with Eq. 4. For large unidirectional displacements the calculation can be considered to work adequately in any case.

The calculated tip force can now be compared with other penetration tests using pile-like structures. [8] for example presented in-situ experiments using an instrumented pile. For smaller scales, similar effects were observed and discussed in [2, 3]. The occurrence of two basic pile driving modes was shown, named cavitational and non-cavitational pile driving. The schematic illustration of these two modes is given in Fig. 11. Figure 11a illustrates the case of non-cavitational and Fig. 11b the case of cavitational pile driving.

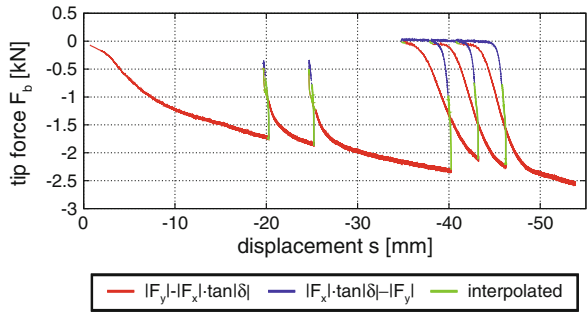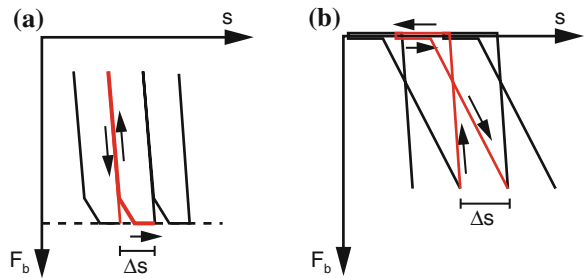**Fig. 10** Estimation of the tip force F_b in test V14-4

Fig. 11 **a** Non-cavitational and **b** cavitational pile driving [2]

Comparing Figs. 10 and 11, it can easily be seen that in the small cycles non-cavitational and in the large cycles cavitational pile driving occurs. For non-cavitational pile driving even in the highest point pull-up phase of the pile a small tip force remains. The stress ratio of the soil elements under the pile tip does not reverse. The deformations in the pull-up phase are relatively small. Therefore, the soil behavior in the penetration phases is very stiff and the tip force rapidly reaches a maximum value. In the test results, this maximum value is not observed but the approaching to a straight increasing line. This difference can be explained considering the boundary conditions in the test device where the pile tip approaches to the rigid bottom plate during the penetration. In the larger cycles in Fig. 10 as well as in Fig. 11b the tip force, ergo the vertical stress in the soil elements under the pile tip, vanishes in the phase of the displacement upwards. The stress ratio reverses and large soil deformations occur. This leads to a much softer response in the subsequent penetration phase. In the experiments and field tests in [2, 3], the soil zone under the pile tip was not visible and the soil deformations could not be evaluated. The test results presented here show that the attribute "cavitational" for this driving mode was justified because a cavity actually occurs under the pile tip in certain conditions.

3.3 Configuration III: 2D Cavity Expansion

The test configuration II is not explicitly suitable for simulation using FEM because the 2D pile tip provides edges of 90° and for simulations smoothed geometries are
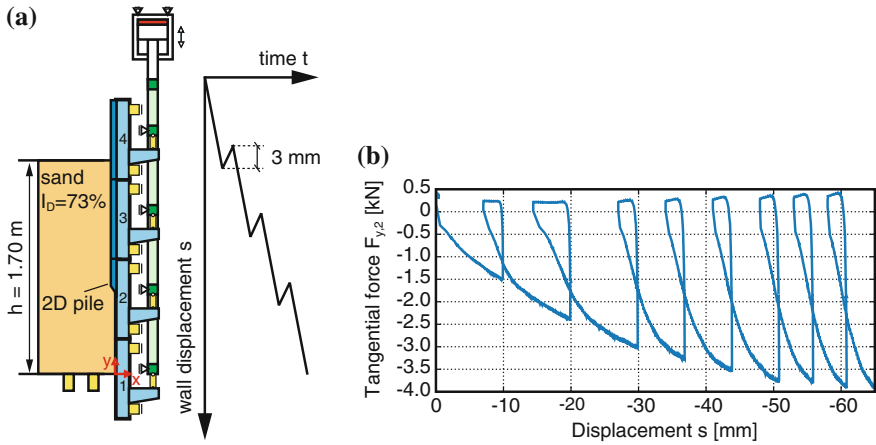
Fig. 12 **a** Initial conditions and test path V15-4 and **b** tangential force $F_{y,2}$ over wall displacement

desirable. Configuration III fits better in these requirements. The pile tip is inclined, sharp edges are avoided and the surfaces of the wall segments are smooth. Thus, the tests performed with this configuration are particularly suitable for simulations. This paper only gives an exemplary overview of the results obtained from DIC analysis. The test path and the initial conditions are shown in Fig. 12a. The test path (Fig. 12a) is an alternating penetration of 65 mm. In the pull-out phases, the displacement upwards is 3 mm, except in the second cycle (about 4 mm). Figure 12b shows the tangential force $F_{y,2}$ on segment 2 over the wall displacement.

Compared to the test presented using configuration II, the evolution of the tangential force $F_{y,2}$ in Fig. 12b indicates a rather cavitational pile penetration. The tangential force increases in the penetration phases and reaches about 3.8 kN after 60 mm wall displacement. The envelope curve in these phases is not linear, but increases gradually. After a strong amount in the beginning of the test, the tangential force increases slowly at the end of the test. In the pull-out phases, a small positive value is reached rapidly. With restarting penetration, the tangential force increases slowly over about 8 mm displacement before it reaches the envelope curve. This behavior is similar to the cavitational pile driving mode shown above. Note that with this test configuration, the inclined pile tip never loses contact to the sand at any time. However, the contact pressure vanishes and the behavior is similar to the cavitational pile driving.

Figure 13 shows the soil displacements obtained from DIC analysis after (a) 20 and (b) 50 mm wall penetration. The contour plots including isolines show the magnitude of the displacements in three areas between the horizontal steel beams. For better orientation, the steel beams that hide parts of the glass windows are illustrated in grey and the initial positions of the four wall segments in blue.
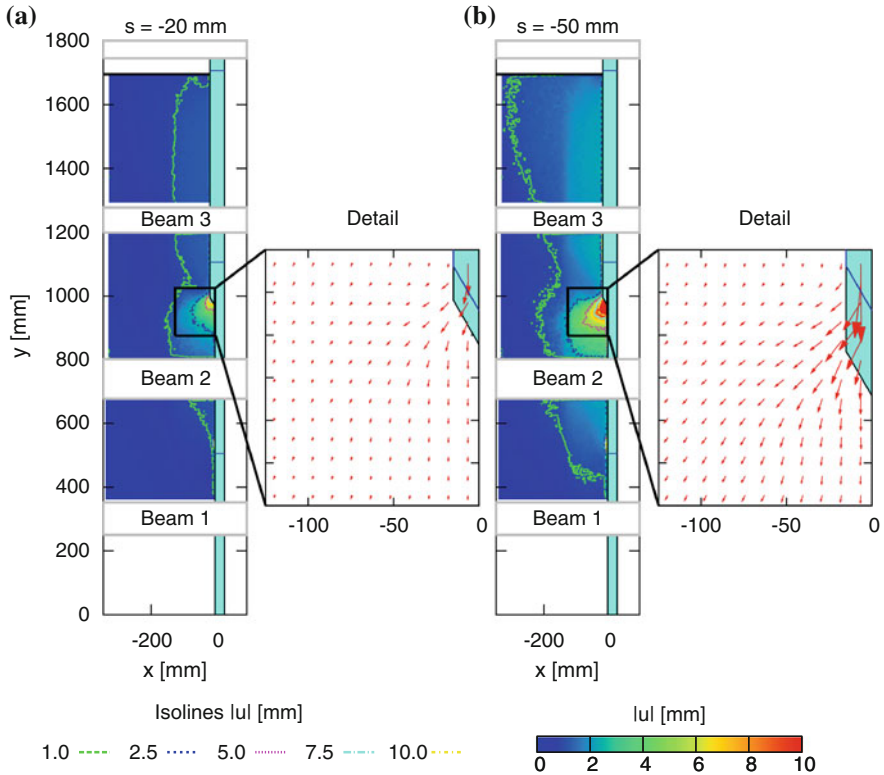
Fig. 13 Displacement magnitudes and vectors for **a** s = −20 mm and **b** s = −50 mm

Beside these information on the displacement magnitudes, vector plots indicate the direction of the displacements in the zone of interest around the pile tip. In order to give a clear overview, not all displacement vectors are shown.

Figure 13a indicates a bulb-like zone of large soil displacements close to the pile tip. This zone extends over about two times the pile diameter from the pile axis. The largest soil displacements are about 8 mm. The complete zone with displacements induced by the pile penetration is about four times as wide as the pile diameter. From the vector plot detail it can be seen that the pile tip displaces the soil particles laterally downwards in the zone adjacent to the inclined pile tip. Under the pile, the displacements are more directed downwards. After 50 mm of penetration, the affected soil zone spreads over the whole width of the glass window. The zone with large displacements has widened too and is more than four times as wide as the pile diameter. The largest displacement is about 25 mm. The 1 mm isoline shows a distinct necking slightly above the pile tip. This can be explained by the penetration of pile volume and the dilative soil behavior in vicinity to the pile tip. Both cause slight displacements upwards above.

4 Summary and Conclusions

Representative results of large scale model tests on important aspects of pile penetration are shown. The tests are designed as boundary value problems for the validation of numerical simulations. An innovative large scale test device is used to perform cyclic and monotonic penetration tests of planar and non-planar wall structures. These structures imitate pile penetrations in dry sand under laboratory conditions (near to plane strain). The distribution of tangential and normal forces on the pile structure is measured. The soil displacements are obtained from DIC analysis. Thus, a holistic impression of the test is provided, which allows an extensive comparison of experiments and simulations.

Tests using three different configuration are discussed. The first test configuration investigates the soil-pile interface using a planar wall structure displaced along an adjacent sand body. These tests clearly show the soil behavior of rough soil-pile interfaces. The influence of the loading on the development of shear zones is pointed out. In monotonic tests, the localization of shear deformations occurs earlier than in cyclic penetration tests. The results represent an important database for the development and the validation of constitutive soil models and contact formulations.

The test configurations II and III concentrate on the soil behavior around pile tips. The occurrence of the pile driving modes, cavitational and non-cavitational pile driving, is demonstrated in the model tests. It is shown that, for flat-ended pile tips, in the case of the cavitational pile driving mode, a cavity forms under the pile tip and in the case of the non-cavitational pile driving not. However, for the acute-angled pile tip in test configuration III no cavity is observable although the pile driving modes are investigated. This leads to the assumption that the cavity is not required for the cavitational pile driving but only the vanishing of the contact stress under the pile tip.

From the test results, the general suitability of the tests to provide similar processes to real pile driving is demonstrated. The wide range of application of the test device and the abilities of the instrumentation for the evaluation of stresses and soil displacements have been pointed out. The experimental database is thus available for Benchmark tests of numerical simulations. In the research unit FOR 1136 the other subprojects can now use these test data for the validation of their work.

References

1. Aubram, D.: *An Arbitrary Lagrangian-Eulerian Method for Penetration into Sand at Finite Deformation*. In: Veröffentlichungen des Grundbauinstitutes der Technischen Universität Berlin, vol. 62. (Shaker, Aachen, 2013)
2. Cudmani, R.O., Huber, G., Gudehus, G.: Zyklische und dynamische Penetration nichtbindiger Böden. Contribution to the Workshop "Boden unter fast zyklischer Belastung", Bochum (2000)
3. Cudmani, R.O.: Statische, alternierende und dynamische Penetration in nichtbindigen Böden. Diss., Veröffentlichungen des Instituts für Bodenmechanik und Felsmechanik der Universität Fridericiana in Karlsruhe, vol. 152 (2001)
4. Dührkop, J., Grabe, J.: Verbesserter Vertikallastabtrag durch konische Pfähle—Feldversuche und Vorschlag für ein Bemessungsverfahren. Bautechnik **85**(11), 748–751 (2008)
5. Finno, R.J., Rechenmacher, A.L.: Effects of consolidation history on critical state of sand. J. Geotech. Geoenviron. **129**(4), 350–360 (2003)
6. Grabe, J., Dührkop, J., Henke, S., Kinzler, S., König, F.: Pfähle mit veränderlichem Querschnitt—konische Pfähle, Fertigteilpfähle mit Fußaufweitung und Flügelpfähle. In: Tagungsband zum Pfahl-Symposium 2007, Mitteilungen des Instituts für Grundbau und Bodenmechanik der TU Braunschweig, vol. 84, pp. 131–155 (2007)
7. Gudehus, G., Nübel, K.: Evolution of shear bands in sand. Géotechnique **54**(3), 187–201 (2004)
8. Huber, G.: Vibrationsrammen: GroßmaSSstäbliche Versuche. Contribution to the Workshop "Vibrationsrammen", Karlsruhe (1997)
9. Kempfert, H.-G., Thomas, S.: Pfahltragverhalten infolge zyklisch axialer Belastung- Versuchsergebnisse und Modellbildung. Tagungsband zur 31. Baugrundtagung der DGGT in München, pp. 255–261 (2010)
10. Rebstock, D.: Verspannung und Entspannung von Sand entlang von Baukörpern. Diss., http://digbib.ubka.uni-karlsruhe.de/volltexte/1000023891
11. Rechenmacher, A.L., Saab, N.A.: Digital Image Correlation (DIC) to evaluate progression and uniformity of shear bands in dilative sand. In: 15th ASCE Engineering Mechanics Conference. Columbia University, New York (2002)
12. Vennemann, P.: JPIV-software package for particle image velocimetry. http://www.jpiv.vennemann-online.de (2007)
13. Vogelsang, J., Huber, G., Triantafyllidis, Th: A large scale soil-structure interface testing device. Geotech. Test. J. **36**(5), 613–625 (2013). doi:10.1520/GTJ20120213, ISSN 0149-6115
14. Walz, B.: Der 1g-Modellversuch in der Bodenmechanik—Verfahren und Anwendung. Vortrag zum 2. Hans Lorenz Symposium, Veröffentlichung des Grundbauinstituts der Technischen Universität Berlin, Heft 40, pp. 13–26 (2006)
15. Westerweel, J.: Digital particle image velocimetry—theory and application. Dissertation, Delft University (1993)
16. White, D.J., Take, W.A.: Particle image velocimetry (PIV) software for use in geotechnical testing. CUED/D-SOILS/TR322 report (2002)